Potential Structure and Propellant Flow Rate Theory for Ion Thruster Discharge Cathode Erosion

IEPC-2005-022

Joshua L. Rovey[*] and Alec D. Gallimore[†]
The University of Michigan, Ann Arbor, MI. 48109, USA

Daniel A. Herman[‡]
QSS Group, Inc., Cleveland, OH. 44135, USA

Abstract: **An ion thruster discharge cathode assembly (DCA) erosion theory is presented based on near-DCA NSTAR plasma potential measurements and experimental results for propellant flow rate effects on ion number density. The plasma potential structures are utilized in an ion trajectory algorithm to determine the location and angle at the DCA keeper of bombarding ions. These results suggest that the plasma potential structure causes a chamfering of the DCA keeper orifice. Results from a diagnostic cylinder (DC) inside a multiple-cathode discharge chamber show that increasing DC propellant flow rate causes a decrease in "keeper" orifice ion number density, most likely due to charge-exchange and elastic collisions. Combining these two results, the known wear-test and extended life test (ELT) DCA erosion profiles can be qualitatively explained. Specifically, the change in the wear profile from the DCA keeper downstream face to the keeper orifice for the ELT may be a result of the reduction in DCA propellant flow rate when the thruster operating point is changed from TH15 to TH8.**

Nomenclature

A	=	Keeper orifice area (m^2)	$\dot{m}_{sccm}$	=	Mass flow rate (sccm)
$\vec{B}$	=	Magnetic field (T)	n_i	=	Ion number density (m^{-3})
$\vec{E}$	=	Electric field (V/m)	n_n	=	Neutral number density (m^{-3})
E_a	=	Axial electric field component (V/m)	p	=	Neutral pressure (Pa)
E_i	=	Impacting ion energy (eV)	q	=	Ion charge (Coulombs)
E_r	=	Radial electric field component (V/m)	T	=	Neutral temperature (K)
$\vec{F}$	=	Force (N)	t	=	Time (s)
I_d	=	Discharge current (A)	u	=	Neutral velocity (m/s)
I_{emag}	=	Electromagnet current (A)	V_d	=	Discharge voltage (V)
j	=	Initial ion current density (A/m^2)	V_p	=	Plasma potential (V)
j_z	=	Attenuated ion current density (A/m^2)	$\vec{v}$	=	Velocity (m/s)
K_0, K_1, K_2	=	Exponential fit coefficients	v_a	=	Axial velocity component (m/s)
m_i	=	Ion mass (2.18x10^{-25} kg)	v_i	=	Average ion velocity (m/s)
$\dot{m}$	=	Mass flow rate (kg/s)	v_r	=	Radial velocity component (m/s)

---

[*] Graduate Student, Department of Aerospace Engineering, jrovey@umich.edu.
[†] Professor, Department of Aerospace Engineering, rasta@umich.edu.
[‡] Research Engineer, On-board Propulsion Branch, Daniel.A.Herman@grc.nasa.gov.

1

$\vec{x}$	=	Spatial location (m)	z	=	Attenuation path length (m)
x_a	=	Axial location (m)	λ_{CEX}	=	Charge-exchange mean free path (m)
x_r	=	Radial location (m)	s_{ce}	=	CEX collision cross section (m^2)
Y	=	Sputtering yield (atoms/ion)	q	=	Impacting ion angle (degrees)

Acronyms

5PLPF	5 planar Langmuir probe with propellant flow	MFP	Mean free path
CEX	Charge-exchange	Mo	Molybdenum
DC	Diagnostic cylinder	NSTAR	NASA solar electric propulsion technology and applications readiness
DCA	Discharge cathode assembly		
ELT	Extended life test	PEPL	Plasmadynamics and electric propulsion laboratory
LVTF	Large vacuum test facility		
MCDC	Multiple-cathode discharge chamber	PLP	Planar Langmuir probe
		TA	Test article

I.   Introduction

Ion thrusters are high-specific impulse, high-efficiency advanced space propulsion systems that are being proposed as the primary propulsion source for a variety of ambitious, long-term, deep space missions. Specifically, missions will require thruster operational lifetimes on the order of 7-14 years.[1-3] Contemporary ion thruster technology utilizing molybdenum discharge cathode keepers is incapable of providing these extended lifetimes due to discharge cathode erosion, which limits the operational life to approximately 3-5 years.[4-6] Therefore the forefront of ion thruster research is concerned with determining these erosion mechanisms and developing methods of eliminating or mitigating them.

Erosion of the NASA Solar Electric Propulsion Technology and Applications Readiness (NSTAR) discharge cathode has been noted in three wear tests performed on a 30-cm engine and an extended life test (ELT) on the flight spare Deep Space One ion engine.[4,5,7-13] During the first wear test, erosion of the discharge cathode was noted,[7] and the engineering solution was to utilize a sacrificial keeper maintained at an intermediate potential between the discharge cathode and anode. The subsequent 1000-h and 8200-h wear tests showed erosion of the discharge cathode assembly (DCA) keeper occurring primarily from the downstream keeper face at approximately the 50% keeper radius, as shown in Figure 1.[8] However, during the ELT, the primary erosion location changed from the keeper downstream face to the keeper orifice. An experimental investigation by Kolasinski found evidence that the
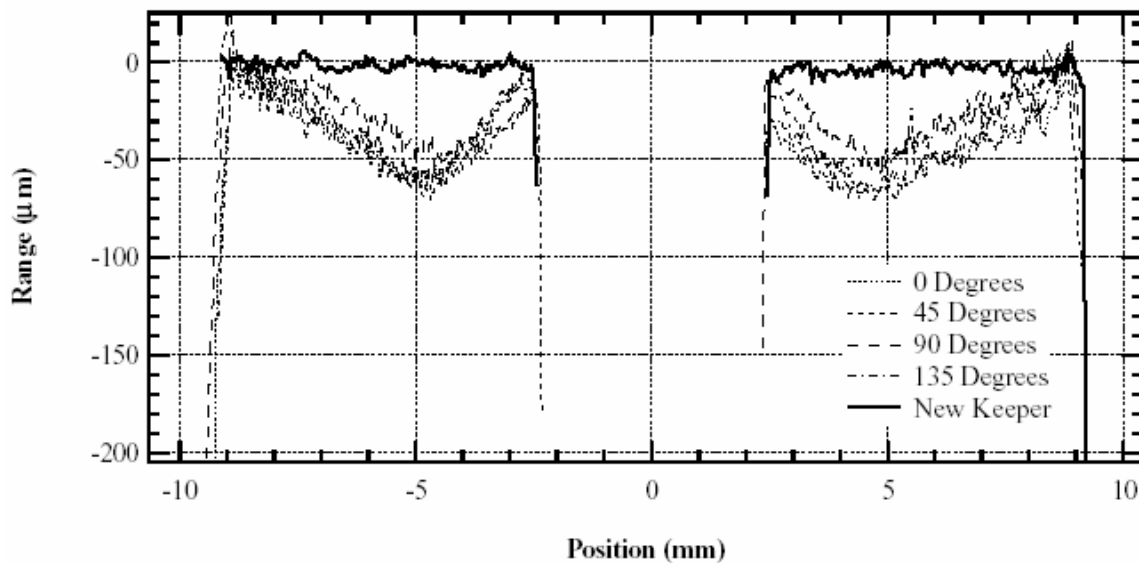

Figure 1: Measured profiles of DCA keeper downstream face for the 1,000-h wear test, conducted primarily at TH15. Note that the maximum erosion occurs at ~50% keeper radius.[8]

Operating Point	Input Power[a] (kW)	Beam Current[b] (A)	Beam Voltage[b] (V)	Accelerator Voltage (V)	Main Flow (mg/s)	Discharge Cathode Flow (mg/s)
TH0[c]	0.5	0.51	650	-150	0.58	0.24
TH4[c]	1.0	0.71	1100	-150	0.81	0.24
TH8[c]	1.4	1.10	1100	-180	1.40	0.24
TH10[c]	1.7	1.30	1100	-180	1.67	0.25
TH12[c]	1.8	1.49	1100	-180	1.79	0.26
TH15[c]	2.3	1.76	1100	-180	2.27	0.36

[a]Nominal values. [b]Power supply current or voltage. [c]Nominal NSTAR operating condition.

Table 1:   Selected NSTAR ion thruster nominal operating parameters.

erosion location shifted when the thruster was operated at a reduced beam current condition; i.e., when the thruster was adjusted from the nominal high-power TH15 condition to the lower-power TH8 operating point.[14,15] Nominal operating conditions for the NSTAR thruster are shown in Table 1. Note the reduction in DCA flow from TH15 to TH8.

The following sections describe an ion thruster DCA erosion theory based on near-DCA NSTAR plasma potential measurements and experimental results for propellant flow rate effects on ion number density. An ion trajectory analysis algorithm based on the NSTAR plasma potential structure for TH8 and TH15 is developed to determine the bombarding ion location and angle at the DCA keeper. A diagnostic cylinder (DC) is designed and operated inside a multiple-cathode discharge chamber (MCDC) to determine the effect of propellant flow rate on "keeper" orifice number density. Finally, the results from these two analyses are combined to form a theory that qualitatively explains the erosion patterns in the wear-test and ELT results.

II.   Erosion Profile Simulation

Erosion profile simulations are completed to determine how the near-DCA plasma potential structures are contributing to the known DCA erosion. Specifically the trajectories of ions in the discharge chamber are computed utilizing simple force equations and experimental plasma potential maps provided by Herman.[16] The following
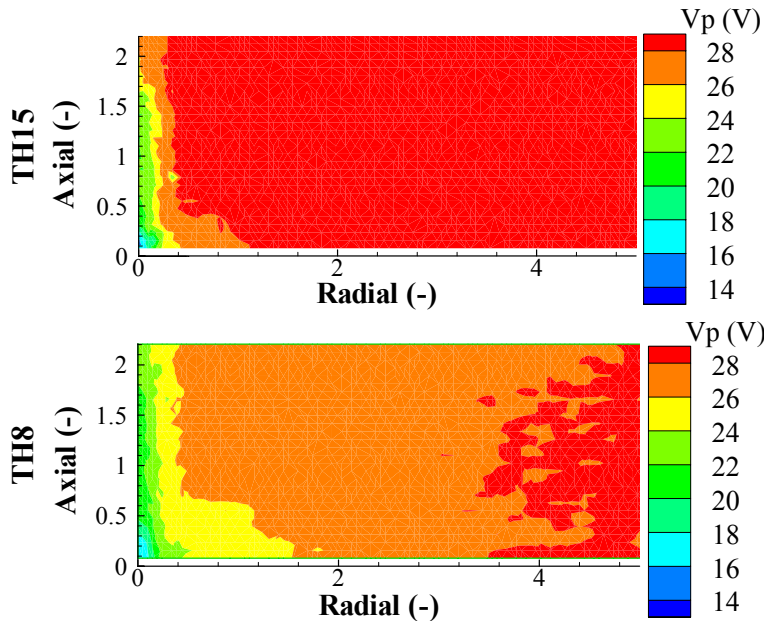
Figure 2: Experimentally measured plasma potential profile in the near-DCA region of the NSTAR ion thruster for TH15 and TH8. Spatial locations are non-dimensionalized with respect to discharge cathode keeper outer diameter.

sections describe the two main components of the erosion profile simulator and the simulation results. The erosion profile simulator is divided into two parts: 1) calculation of the ion trajectory to determine bombarding ion impact angle and location on the keeper downstream face; and 2) an erosion calculation (i.e., how many atoms are sputtered per incident ion) using the calculated impact angle and known bombarding ion energy. Combining these two steps allows a simulated keeper erosion profile to be determined.

A. Ion Trajectory Calculation

An ion trajectory calculation compiled using MatLab is utilized to determine the bombarding ion impact angle and location at the keeper downstream face. The trajectory simulation procedure is similar to that used by Beal[17] and is divided into five main steps: 1) load the plasma potential maps provided by Herman;[16]

2) calculate the electric field produced by the variation of plasma potential with spatial location; 3) determine initial conditions for a simulation ion; 4) iteratively calculate the ion trajectory based on the initial conditions; and 5) determine if the ion impacts the keeper and, if so, determine the impact location and angle.

Initially the near-DCA plasma potential structures measured by Herman[16] are loaded. The plasma potential structures associated with TH15 and TH8 are shown in Figure 2. The 2-D area over which the data are plotted is initially reduced to create a rectangular region shown in Figure 3. This domain size is chosen because plasma potential data are only available in this region and computationally the analysis is simplified for a rectangular domain. For more information regarding the plasma potential structures see Ref. 16 and 18. Next the data are interpolated onto a 1 mm by 1 mm grid such that the entire computational domain has 4400 grid points. Because a certain amount of noise is present in the raw plasma potential data, the built-in MatLab cubic smoothing spline algorithm is used to smooth the data. An example of the raw and smoothed data is shown in Figure 4. Next the electric field is calculated within the computational domain.

Figure 3: Schematic of an ion thruster showing the computational domain over which the ion trajectories are computed. Not to scale.

The electric field at a given point is determined using the plasma potentials at the six adjacent points and Eq. 1,[19] where V_p is plasma potential, $\vec{E}$ is electric field, and $\vec{x}$ is the relative position between grid points.

$$\vec{E} = -\frac{dV_p}{d\vec{x}} \qquad (1)$$

Figure 4: Comparison of raw and smoothed data for TH15. Spatial locations are non-dimensionalized by the discharge cathode keeper diameter.

Table 2 shows the ion initial conditions investigated. A single simulation has 35,200 ions with 4400 initial positions (an ion starts from each of the computational domain grid points) and 8 initial angular orientations. Angular orientations of 0 degrees and 90 degrees correspond to an initial velocity in the positive radial and positive axial directions, respectively. Simulations are completed for both warm and cold ions, as well as singly- and doubly-charged ions. Warm and cold ions are assumed to have energies of 5 eV and 0.05 eV, respectively.[6]

Utilizing the provided initial conditions, the ion trajectory is calculated by iterating through the familiar Lorentz force equation, Eq. 2.

Locations	4400 points (Dx = 1.0 mm)
Charge-state	singly, doubly
Initial Energy (eV) (velocity)	Warm (5 eV) Cold (0.05 eV)
Anglular Orientation (deg.)	0, 45, 90, 135, 180, 225, 270, 315

Table 2: Ion initial conditions

$$\vec{F} = q(\vec{E} + \vec{v} \times \vec{B}) \qquad (2)$$

In this equation, $\vec{F}$ is the force on the ion, $\vec{E}$ is the electric field, $\vec{v}$ is the ion velocity, q is the ion charge, and $\vec{B}$ is the magnetic field. For the simulations presented here, the magnetic field inside the ion thruster is assumed to have a negligible impact on ion motion and therefore the Lorentz equation can be reduced and divided into axial and radial components as shown in Eq. 3, where Newton's relation for force and acceleration has also been used.[19]
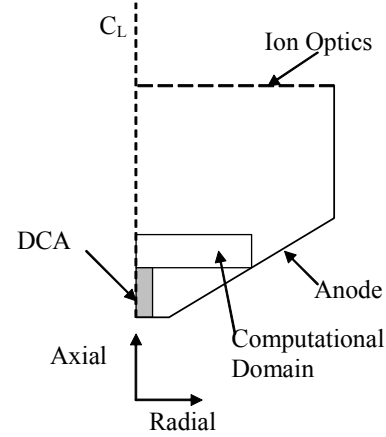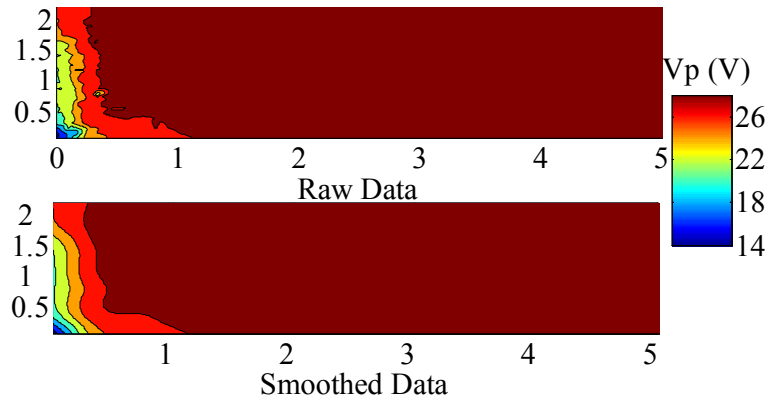
$$\left(\frac{dv}{dt}\right)_a = \frac{qE_a}{m_i}$$

$$\left(\frac{dv}{dt}\right)_r = \frac{qE_r}{m_i}$$

(3)

In these equations, v_a and v_r are the ion velocity in the axial and radial directions, respectively, t is time, q is the ion charge, E_a and E_r are the axial and radial electric field, respectively, and m_i is the ion mass. Lastly, Eq. 4 is utilized as the relation between spatial location and velocity, where x_a and x_r are the axial and radial position, respectively.[19]

$$v_a = \left(\frac{dx}{dt}\right)_a$$

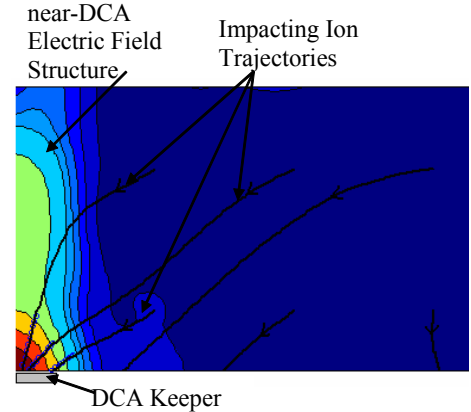$$v_r = \left(\frac{dx}{dt}\right)_r$$

(4)

Figure 5: Example ion trajectories through the calculated electric field profile within the computational domain.

Utilizing the equations described above, the trajectory calculation iterative procedure loop is as follows: 1) interpolate the electric field at the ion position (because the ion position is rarely directly on one of the grid points, the electric field values are linearly interpolated from the 4 nearest grid points); 2) calculate the new velocity components using Eq. 3; 3) determine the new spatial location by assuming the new velocity components are constant over the time step; and 4) repeat. This procedure loop is iterated until the ion exits the computational domain (Figure 3). If the ion exit position is at the DCA keeper, then the ion impact location is recorded and the bombarding angle is calculated by fitting a line to previous locations along the trajectory. The inverse tangent of the inverse of the slope of this line provides the impact angle with respect to keeper normal (Note: these are the pre-sheath angle and pre-sheath location). The outputs of the trajectory simulator are the initial location, initial velocity components, pre-sheath impact angle, pre-sheath velocity components, and pre-sheath impact location of ions striking the keeper.

Initial simulations are completed to determine the required time step that provides accurate and timely results. Simulations are completed for values greater than or equal to 1×10^{-9} s. Comparison of the output results show that time steps of 1×10^{-7} s and smaller yield identical trajectories. Therefore a time step of 1×10^{-7} s is used for all simulations reported here. Examples of ion trajectories through the calculated electric field profile are shown in Figure 5. Note that three of the six ions impact the keeper.

B. Erosion Calculation

The results of the trajectory simulations provide the pre-sheath impact angle, pre-sheath velocity components, and pre-sheath impact location of ions striking the DCA keeper. However, ions first pass through the keeper sheath before impacting, so the through-sheath impact location, angle, and energy must be determined. An ion is assumed to only translate axially through the sheath, so the through-sheath impact location is equivalent to the pre-sheath location. This assumption is justified by the small thickness of the sheath and small radial electric fields expected within the sheath. Pre-sheath radial velocity is assumed constant through the sheath and the axial velocity component is assumed to increase corresponding with the gain in energy through the keeper sheath potential drop. The angle of the sum of these two velocity components is the through-sheath impact angle. The near-DCA plasma potential (~14 V) and floating keeper potential (~5 V) are used to determine the keeper sheath potential drop of ~9 V. Bombarding ion energy is calculated as the ion kinetic energy using the through-sheath velocity components.

The keeper erosion profile is predicted utilizing the through-sheath impact angle, location, and velocity components. Calculation of an erosion profile requires either an accurate sputtering yield model or, in this case, experimental sputtering yield data. Sputtering yield, Y, is a statistical variable defined as the mean number of atoms removed from a solid target per incident particle. In this application, the sputtering yield indicates the mean number of molybdenum (Mo) atoms removed from the keeper face per incident xenon ion.

Doerner, *et al.*, measured Mo sputtering yields during xenon ion bombardment in the energy range of 10 to 200 eV utilizing the standard weight loss and spectroscopic techniques.[20] These results compare nicely to each other and

to existing low-energy Xe$^+$-Mo data taken by other researchers.[20] These experimental data are the low-energy normal-incidence sputtering yields that are utilized as the basis for the erosion calculations. The Doerner data are log-log plotted and a sixth order polynomial fit to the resulting graph provides an empirical relation for sputtering yield (Y) and normal-incident bombarding ion energy (E_i), Eq. 5.

$$Y_{Doerner}(E_i) = \exp\{-0.372304[\ln(E_i)]^6 + 9.48041[\ln(E_i)]^5 - 100.046[\ln(E_i)]^4$$
$$+ 560.276[\ln(E_i)]^3 - 1758.24[\ln(E_i)]^2 + 2940.48[\ln(E_i)] - 2064.3\}$$

(5)

$$\left(\frac{Y(\theta)}{Y(0)}\right) = \cos^{-19.96}(\theta) \cdot \exp[-13.55(\cos^{-1}(\theta)-1)]$$

(6)

An empirical formula for the angular dependence of the sputtering is given by Yamamura, *et al.*, as Eq. 6.[21,22] The numeric factors are energy-dependent fit parameters determined from 100 eV xenon ions impacting a Mo target and Y(0) is the sputtering yield at normal incidence, i.e., Eq. 5.[22] Previous use of this erosion analysis algorithm has been applied with success by Herman.[18]

C. Simulation Results

Simulation results are for singly- and doubly-charge ions, as well as cold and warm ion populations. Figure 6 shows simulated erosion profiles for the warm and cold ion assumptions for the TH15 and TH8 NSTAR thruster operating conditions. The doubles-to-singles ratio in the NSTAR thruster is a function of the operating condition and is expected to be within 20-25%.[23] For this analysis the ratio is assumed to be a constant equal to 20%, so each erosion profile shown is the sum of 80% of the singly-charged profile and 20% of the doubly-charged profile. Doubly-charged ions tend to increase the magnitude of the profile, but have no affect on the shape. The warm ion assumption predicts less erosion of the keeper than the cold profile because higher-energy, warm ions are capable of escaping from the near-DCA low plasma potential region, while less-energetic, cold ions are more easily pulled into the keeper by the potential field. Because the discharge chamber plasma contains a distribution of ions, the true erosion profile is assumed to be some combination of the warm and cold ion results.

Both the TH15 and TH8 results predict an erosion profile that leads to chamfering of the keeper orifice. The increase in erosion at the keeper orifice (~25% keeper radius) leads to a chamfering profile that causes the orifice diameter to increase until the entire keeper face is eroded. This analysis suggests that the plasma potential structure produced by the coupling of the DCA with the bulk plasma causes the primary erosion location to be at the DCA keeper orifice. Results from the 1,000-h and 8,200-h wear-tests show the dominant erosion location to be at approximately the 50% keeper radius location (Figure 1), not the keeper orifice. Therefore the plasma potential structure alone can not be causing the known erosion results.
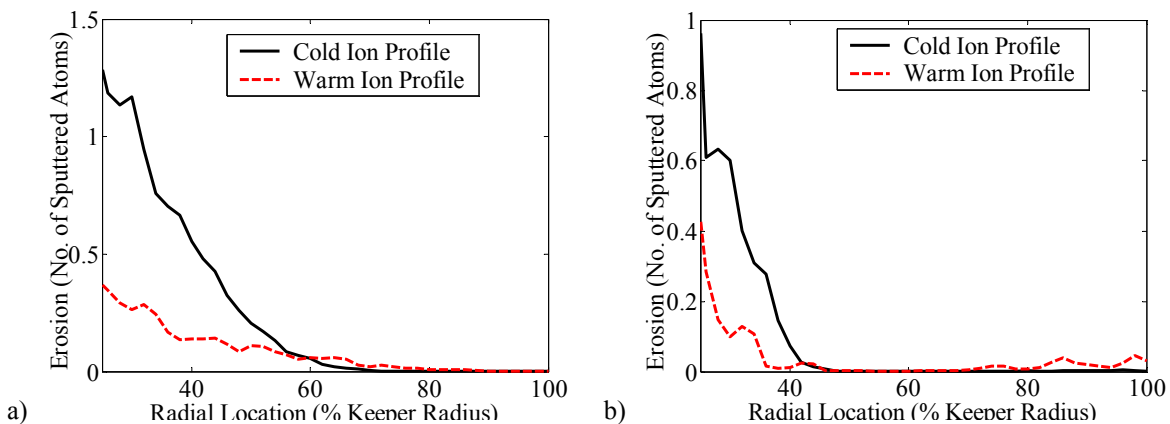

Figure 6: Simulated erosion profiles for the warm and cold ion assumptions for a) TH15 and b) TH8 NSTAR plasma potential maps.

III. Propellant Flow Rate Effects

A MCDC test article (TA)[24,25] is used to predict the effects of propellant flow rate on near-DCA plasma properties. The TA is a rectangular discharge chamber designed to increase thruster life by operating three sequential DCAs. Therefore, at any time, the TA contains an active DCA and two dormant cathodes. For the experiment presented here an active NEXT-DCA and two DCs are attached to the TA. Each DC appears similar in size and shape to the active DCA, but is outfitted with plasma diagnostics to analyze the dormant cathode plasma properties. Specifically, each DC is outfitted with 5 planar Langmuir probes (PLP) and is capable of propellant flow (5PLPF). These devices allow the effects of propellant flow on dormant cathode plasma properties to be studied. During data acquisition, as the DC propellant flow is increased the main plenum flow rate is decreased such that the total propellant flow rate is constant. This also ensures that the TA performance properties are maintained. The Plasmadynamics and Electric Propulsion Laboratory (PEPL) Large Vacuum Test Facility (LVTF) at the University of Michigan is used for all experiments.

Figure 7: Photograph of a 5PLPF-DC. Note the 5 planar Langmuir probes and propellant flow exhaust "keeper" orifice. This is not an active DCA.

A. 5PLPF-DC

Two 5PLPF-DCs are fabricated to make plasma property measurements at the two dormant cathode locations internal to the TA. Each DC appears similar to the active NEXT-DCA, however, each DC "keeper" is outfitted with 5 PLPs at different spatial locations as shown in Figure 7. A stainless steel "keeper" is attached to a Macor insulator to form the base of the DC. The 5PLPF-DCs do not contain a "cathode" electrode. Ten PLPs are constructed of 0.08 cm (0.031") diameter tungsten wire

Figure 8: Internal schematic of 5PLPF-DC. Propellant enters off-axis and is then transferred to the "keeper" orifice by a small channel.

surrounded by a 0.16 cm (0.063") outer diameter alumina tube yielding a probe area of 0.50 mm². Each PLP is inserted axially into the DC such that the probe collecting surface is flush with the "keeper" faceplate. 5 PLPs are placed into each of the two DCs in a symmetrical pattern with each probe spaced 0.64 cm (0.25") from the centerline axis. Ceramic epoxy is utilized to construct the probes, as well as to mate the probes, "keeper", and Macor insulator. An aluminum mounting flange is utilized to attach the DC to the TA at one of the dormant cathode locations. Finally, a 3.2 mm (0.125") outer diameter tube is inserted off-centerline into the DC to feed propellant through the "keeper" orifice. A small internal channel is used to transfer the off-axis propellant tube exhaust to the "keeper" orifice. A schematic of this setup is shown in Figure 8. Electrically each of the 5PLPF-DCs is operated identically to the DCs described in Ref. 25 and the Langmuir probe data analysis technique is also identical.

B. Results

Data are obtained for a variety of TA operational configurations and the configuration nomenclature is shown in the Appendix. The 5PLPF-DC trends due to adjustment of the magnetic field, DCA location, and DC connectivity are consistent with previous investigations.[25] Of primary interest for the discussion presented here is the effect of DC propellant flow on ion number density at the DC "keeper" orifice and downstream face. Results obtained with the probe located in the "keeper" orifice are discussed first.

Results reported in Figure 9-a are for probe 14, which is located at the "keeper" orifice of the DC on the right side of the TA for all experiments. Results indicate that the number density at the DC orifice decreases approximately 20% when the DC propellant flow is adjusted from zero to the full DCA flow rate. The number density results are of particular interest because the flow appears to be shielding the DC from bombarding ions, a result consistent with a previous investigation.[24] *Therefore TA dormant cathodes should be operated with propellant flow in order to reduce the number of ions bombarding those units and causing pre-operation erosion.* Perhaps the pre-operation wear of the dormant cathodes can be reduced by as much as 20% by operating the units with propellant flow.
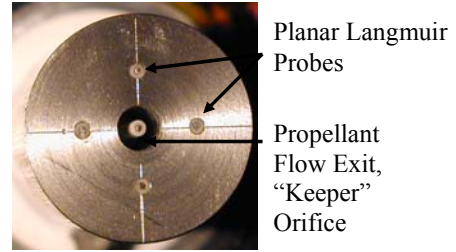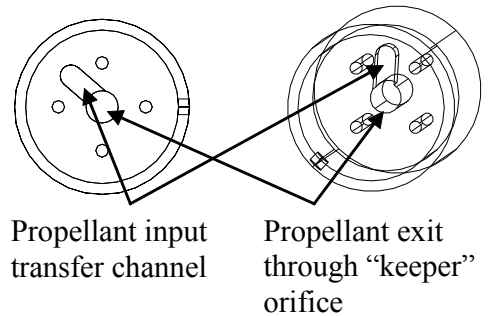
Results from the probes located at different locations on the DC "keeper" face plate (probe 10, 11, and 13) do not show the same trend in ion number density as the "keeper" orifice probe (probe 14). These results are shown in Figure 9-b. Because the results with the other probes do not show a consistent trend and the ion number density does not increase or decrease as significantly as the "keeper" orifice probe, the effects of the propellant flow are assumed to become negligible at the radial location of these probes. Therefore, at ~50% "keeper" radius from the DC centerline propellant flow no longer has a noticeable effect on the measured number density.

The decrease in DC "keeper" orifice number density may be attributed to elastic and charge-exchange (CEX) collisions, where the latter is known to cause changes in near-DCA ion energy distributions when external flow is present.[26] Elastic collisions may also be present, but have a significantly smaller collision cross-section and are not included in this analysis. Considering the "keeper" orifice bombarding ions as an ion beam with initial current density, j, a first order estimation of the attenuation due to CEX collisions is obtained by considering the ion continuity equation in one dimension. The ratio of the ion current density at some position, j_z, to the initial ion current density is obtained by integrating over the pathlength, z. The result is Eq. 7,[27]

$$\frac{j_z}{j} = \exp(-n_n \sigma_{ce} z) \tag{7}$$

where j_z is the ion current density after the beam has suffered CEX attenuation over a pathlength z, j is the ion current density measured if CEX collisions are not present, n_n is the neutral density, and σ_{ce} is the CEX collision cross-section. Ion current density is related to ion number density through Eq. 8,

$$j = q n_i v_i \tag{8}$$

where j is ion current density, q is the charge of the ions, n_i is the ion number density, and v_i is ion velocity. Assuming the mass flow rate through the DC, $\dot{m}_{sccm}$, is proportional to the neutral density, n_n, the experimental data in Figure 9-a can be fit using a slightly modified form of Eq. 7. The form of the equation fit to the data is shown in Eq. 9,

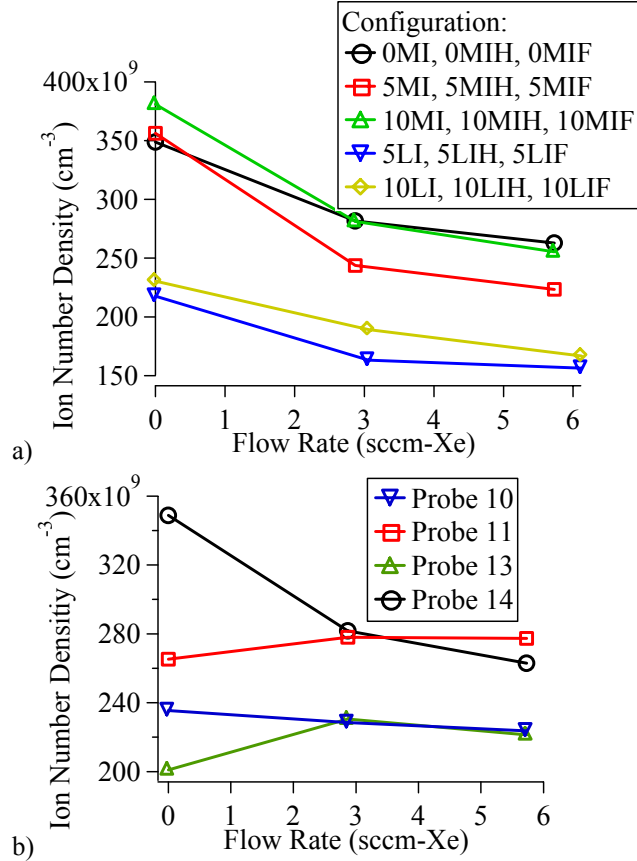$$n_i = K_0 + K_1 \exp(-K_2 \dot{m}_{sccm}) \tag{9}$$

a)

b)

Figure 9: 5PLPF results for a) "keeper" orifice probe (probe 14) for the configurations shown and b) probes with different locations on the right DC for 0MI, 0MIH, and 0MIF TA configurations.
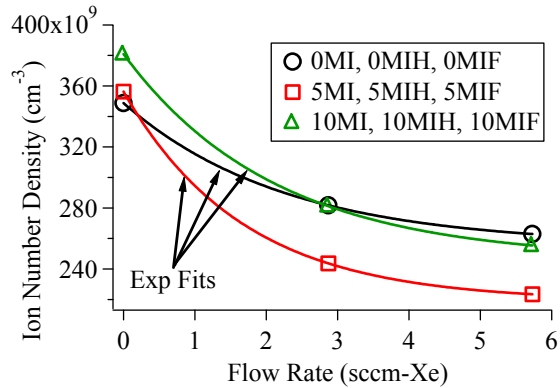
Figure 10: **Exponential fits to the "keeper" orifice probe 14 data for various TA configurations.**

8

Configuration	K_o	K_1	K_2	z/λ_{CEX} $\dot{m}_{sccm} = 3$	z/λ_{CEX} $\dot{m}_{sccm} = 6$
0MI, 0MIH, 0MIF	2.56E+11	9.33E+10	0.442	1.87	3.75
5MI, 5MIH, 5MIF	2.19E+11	1.37E+11	0.597	2.53	5.07
10MI, 10MIH, 10MIF	2.46E+11	1.35E+11	0.471	2.00	4.00

Table 3:   Exponential fit parameters and ratio of the pathlength to the CEX mean free path.

where n_i is ion number density, K_o, K_1, and K_2 are the fit coefficients, and $\dot{m}_{sccm}$ is the flow rate in sccm. The fit coefficients for the three curves shown in Figure 10 are given in Table 3. These fits strongly suggest that CEX collisions are causing the observed trends. However, in order for this analysis to be appropriate the pathlength, z, should be greater than the mean free path (MFP) of a CEX collision. This ensures that multiple CEX collisions are occurring over the integrated pathlength.

The relationship for the CEX MFP is given in Eq. 10,

$$\lambda_{CEX} = \frac{1}{\sqrt{2}n_n\sigma_{ce}}$$ (10)

where λ_{CEX} is the CEX MFP, σ_{ce} is the CEX collision cross-section, and n_n is the neutral density. By setting the exponential of Eq. 7 and Eq. 9 equal, a relationship between the theoretical attenuation equation and the experimental data can be determined. This result is shown in Eq. 11.

$$n_n\sigma_{ce}z = K_2\dot{m}_{sccm}$$ (11)

$$\frac{z}{\lambda_{CEX}} = \sqrt{2}K_2\dot{m}_{sccm}$$ (12)

Combining Eq. 10 and Eq. 11 allows the ratio of the pathlength to the CEX MFP to be determined. The result is shown as Eq. 12. For the flow rates presented here (~3 and 6 sccm) and for the experimentally determined K_2 values, the ratio is typically between 2-5, and the results for the data in Figure 10 are shown in Table 3. These results show that the pathlength is larger than the CEX MFP, suggesting that CEX collisions are responsible for the observed decrease in ion number density with increasing propellant flow rate.

An estimation of the neutral pressure at the DC "keeper" orifice is obtained by considering the continuity equation and the ideal gas law. The result is Eq. 13,

$$p = \frac{\dot{m}RT}{uA}$$ (13)

where p is neutral pressure, u is the neutral velocity at the orifice, A is the orifice area, T is the neutral temperature, $\dot{m}$ is the mass flow rate, and R is the specific gas constant for xenon. Assuming T is 1000 K[28] and the velocity is equal to the sound speed, the pressure is calculated to be ~60 mTorr for the maximum flow rate, which yields a neutral density of 5.5×10^{20} m^{-3}. Furthermore, if the bombarding ions are assumed to have energy equal to the plasma potential (~30 V), σ_{ce} is equal to 45 Å^2 [29] and the CEX MFP and corresponding pathlength, z, are calculated to be 2.9 mm and 14 mm, respectively.

IV.   DCA Erosion Theory

A DCA erosion theory is developed that combines the plasma potential profile ion trajectory simulations and the DC propellant flow rate effects. The following sections use the results presented above to qualitatively predict erosion profiles for the TH15 and TH8 operating conditions, as well as to explain the change in erosion profile between operating points. The theory is then used to explain the ELT erosion results.

One of the key assumptions is that the propellant flow rate results obtained with the 5PLPF-DCs are applicable to the active DCA. The 5PLPF-DCs are not electron emitting devices and are therefore not producing the familiar

near-DCA plasma potential structures. The active DCA keeper may have a different ion number density distribution. However, the goal of this analysis is to develop physical insight into possible erosion producing and erosion mitigating mechanisms using known results. Further investigation and validation of this theory require determining the effects of propellant flow rate on the active DCA keeper ion number density. Therefore the theory presented is purely qualitative, but based on quantitative results from the ion trajectory simulations and the 5PLPF-DCs.

A. TH15

The NSTAR operating condition TH15 is the high-power, high-flow rate condition (Table 1). Figure 11 shows the predicted erosion profile for TH15 and Figure 1 shows the measured erosion profile of the DCA keeper downstream face after the 1,000-h wear test, which operated primarily at TH15.[8] Propellant flow rate results with the DCs suggest that near the DCA keeper orifice, bombarding ion number density is reduced due to CEX collisions. Therefore the erosion at the keeper orifice predicted by the ion trajectory simulation is reduced. As radial distance from the orifice increases, the neutral density and corresponding number of CEX collisions decreases, leading to an increase in erosion. At approximately the 50% keeper radius, the DC results suggest that the effects of propellant flow rate are no longer present. Therefore the 50% keeper radius corresponds to the maximum erosion point. Note that in the 1,000 hour wear test results (Figure 1) the maximum erosion occurs at approximately the 50% keeper radius.[8] At larger radial locations the erosion profile corresponds to the ion trajectory simulation results because propellant flow rate effects are no longer present.
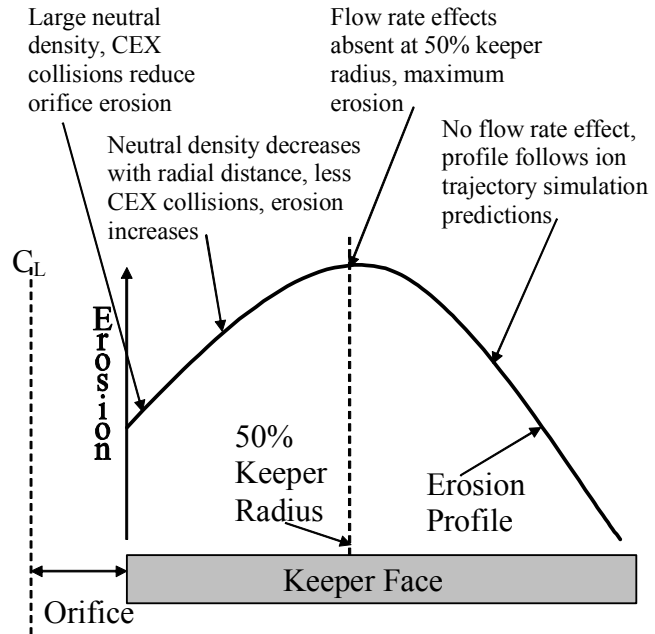
B. TH8

The TH8 NSTAR operating point is lower-power and lower-flow rate than the TH15 point (Table 1). The reduction in DCA flow rate reduces the keeper orifice neutral density and therefore the ability of the DCA to protect itself from bombarding ions through CEX collisions. The TH8 erosion profile is therefore identical to the ion trajectory simulation predicted profiles because flow rate effects and CEX collisions are either not present or significantly reduced. This result is shown in Figure 12.

C. ELT Results Explanation

During the ELT, the NSTAR flight spare engine was operated at various power levels and operating points. Erosion of the DCA keeper orifice began during TH8 after ~6,400-h of operation. The sudden and significant increase in keeper orifice erosion also corresponded with a short between the cathode and the keeper.[5] Herman has shown that the potential structure of the near-DCA plasma does not change when the cathode is shorted to the

Figure 11: Qualitative erosion profile prediction for TH15.

Figure 12: Qualitative erosion profile prediction for TH8.

keeper.[16,18] However, bombarding ions gain more energy through the keeper sheath (the keeper-to-cathode floating potential, 3-7 V) when the cathode is shorted to the keeper, which increases the sputter yield and the erosion rate. The following section uses the DCA erosion theory to explain the ELT results.

At the onset of the ELT, the thruster is operated at TH12 and then TH15, where it suffers erosion at the 50% keeper radius point on the keeper downstream face (TH15 erosion profile, Figure 11). At ~4,500-h into the test, the thruster is adjusted to the lower-power, lower-flow rate TH8 operating point. The erosion profile then shifts due to the change in DCA flow rate and the erosion now occurs at the keeper orifice, leading to a chamfering profile (Figure 12). The cathode-to-keeper short at ~6,400-h only increases the erosion rate, however, the erosion profile is not affected. At ~10,500 hours the thruster is returned to TH15, but the keeper orifice has been eroded to two times its initial diameter. Although the DCA flow rate is increased upon returning to TH15, the keeper orifice is larger so the neutral number density does not return to the pre-TH8 value. Because of the enlarged orifice and corresponding reduced neutral density, the erosion continues with the TH8 profile even though the thruster is operating at TH15. This erosion profile remains the same throughout the remainder of the ELT, eventually eroding away the entire keeper face.

V. Conclusion

A DCA erosion theory is developed based on ion trajectory simulation results and propellant flow rate effects. Ion trajectories are simulated using the plasma potential structure measurements and simple force equations. Results indicate that the plasma potential structures cause a chamfering erosion of the DCA keeper orifice, which eventually causes the orifice to enlarge and the keeper face to be completely eroded. These results are identical for the TH15 and TH8 operating conditions, suggesting that the potential structure along can not be causing the 1,000-h wear-test erosion results. Propellant flow rate effects on a DC in a MCDC TA suggest that increasing flow rate through the DCA may lead to a decrease in orifice bombarding ions due to CEX collisions. The erosion theory combines these two effects to predict erosion profiles for the NSTAR TH15 and TH8 operating conditions. The theory suggests that the lower power, lower flow rate TH8 condition has a linear erosion profile that causes more erosion at the keeper orifice. This profile leads to chamfering of the orifice and eventual loss of the keeper face. The high-power, high flow rate TH15 has a peaked erosion profile with a maximum occurring at approximately the 50% keeper radius point. The theory is consistent with erosion profiles measured after the 1,000 hour wear test[8] and results presented by Kolasinski that suggest the erosion profile changes from TH15 to TH8.[14,15]

The theory suggests that the ELT erosion results are a product of the thruster operating point and the cathode-to-keeper short. Specifically the change in ELT erosion location from the downstream keeper face to the keeper orifice was caused by the decrease in propellant flow rate when the thruster was adjusted from TH15 to TH8 and the increase in erosion rate was caused by the keeper short to the cathode. It may be possible to mitigate keeper orifice erosion by increasing the DCA flow rate when operating at the TH8 condition.

Acknowledgments

References

[1]Katz, I., "Electric Propulsion for JPL Missions," AIAA-2005-3674, *41st Joint Propulsion Conference*, Tucson, AZ, July 10-13, 2005.

[2]Oleson, S*., et al.*, "The Electric Propulsion Segment of Prometheus 1," AIAA-2005-3888, *41st Joint Propulsion Conference*, Tucson, AZ, July 10-13, 2005.

[3]Randolph, T*., et al.*, "The Prometheus 1 Spacecraft Preliminary Electric Propulsion System Design," AIAA-2005-3889, *41st Joint Propulsion Conference*, Tucson, AZ, July 10-13, 2005.

[4]Sengupta, A*., et al.*, "An Overview of the Results from the 30,000 Hr Life Test of Deep Space 1 Flight Spare Ion Engine," AIAA-2004-3608, *40th Joint Propulsion Conference*, Fort Lauderdale, FL, July 11-14, 2004.

[5]Sengupta, A., Brophy, J. R., Goodfellow, K., "Status of the Extended Life Test of the Deep Space 1 flight spare engine after 30,352 hours of operation," AIAA-2003-4558, *39th Joint Propulsion Conference*, Huntsville, AL, July 20-23, 2003.

[6]Domonkos, M. T., Foster, C., Soulas, G. C., "Wear Testing and Analysis of Ion Engine Discharge Cathode Keeper," *Journal of Propulsion and Power*, Vol. 21, No. 1, pp. 102-110, Jan.-Feb. 2005.

[7]Patterson, M. J*., et al.*, "2.3 kW Ion Thruster Wear Test," AIAA-95-2516, *31st Joint Propulsion Conference*, San Diego, CA, July 10-12, 1995.

[8]Polk, J. E*., et al.*, "A 1000-Hour Wear Test of the NSTAR Ion Thruster," AIAA-96-2717, *32nd Joint Propulsion Conference*, Lake Buena Vista, FL, July 1-3, 1996.

[9]Anderson, J. R*., et al.*, "Results of an On-going Long Duration Ground Test of the DS1 Flight Spare Ion Engine," AIAA-99-2857, *35th Joint Propulsion Conference*, Los Angeles, CA, June 20-24, 1999.

[10]Polk, J. E*., et al.*, "An Overview of the Results from an 8200 Hour Wear Test of the NSTAR Ion thruster," AIAA-99-2446, *35th Joint Propulsion Conference*, Los Angeles, California, June 20-24, 1999.

[11]Polk, J. E*., et al.*, "The Effect of Engine Wear on Performance in the NSTAR 8000 Hour Ion Engine Endurance Test," AIAA-97-3387, *33rd Joint Propulsion Conference*, Seattle, WA, July 6-9, 1997.

[12]Sengupta, A*., et al.*, "Performance Characteristics of the Deep Space 1 Flight Spare Ion Thruster Long Duration Test after 21,300 hours of operation," AIAA-2002-3959, *38th Joint Propulsion Conference*, Indianapolis, IN, July 7-10, 2002.

[13]Anderson, J. R*., et al.*, "Performance Characteristics of the NSTAR Ion Thruster During an On-Going Long Duration Ground Test," *IEEE Aerospace Conference*, Vol. 4, pp. 99-122, Big Sky, MT, March 18-25, 2000.

[14]Kolasinski, R. D., Polk, J. E., "Characterization of Cathode Keeper Wear by Surface Layer Activation," *Journal of Propulsion and Power*, Vol. 20, No. 6, pp. 992-999, Nov.-Dec. 2004.

[15]Kolasinski, R. D., Polk, J. E., "Characterization of Cathode Keeper Wear by Surface Layer Activation," AIAA-2003-5144, *39th Joint Propulsion Conference*, Huntsville, AL, July 20-23, 2003.

[16]Herman, D. A., Gallimore, A. D., "Near Discharge Cathode Assembly Plasma Potential Measurements in a 30-cm NSTAR-type Ion Engine amidst Beam Extraction," AIAA-2004-3958, *40th Joint Propulsion Conference*, Fort Lauderdale, FL, July 11-14, 2004.

[17]Beal, B. E., "Clustering of Hall Effect thrusters for High-Power Electric Propulsion Applications," Doctoral Thesis, Dept. of Aerospace Engineering, University of Michigan, Ann Arbor, MI, 2004.

[18]Herman, D. A., "The Use of Electrostatic Probes to Characterize the Discharge Plasma Structure and Identify Discharge Cathode Erosion Mechanisms in Ring-Cusp Ion Thrusters," Doctoral Thesis, Dept. of Aerospace Engineering, University of Michigan, Ann Arbor, MI., 2005.

[19]Halliday, D., Resnick, R., Walker, J., *Fundamentals of Physics*, Fifth Ed., John Wiley & Sons, Inc., New York, 1997.

[20]Doerner, R. P., Whyte, D. G., Goebel, D. M., "Sputtering yield measurements during low energy xenon plasma bombardment," *Journal of Applied Physics*, Vol. 93, No. 9, pp. 5816-5823, May 2003.

[21]Yamamura, Y., "An Empirical Formula for Angular Dependence of Sputtering Yields," *Radiation Effects*, Vol. 80, pp. 57-72, 1984.

[22]Duchemin, O. B*., et al.*, "A Review of Low Energy Sputtering Theory and Experiments," IEPC-97-068, *25th International Electric Propulsion Conference*, Cleveland, OH, August 24-28, 1997.

[23]Williams, G. J., Domonkos, M. T., Chavez, J. M., "Measurement of Doubly Charged Ions in Ion Thruster Plumes," IEPC-01-310, *27th International Electric Propulsion Conference*, Pasadena, CA, October 15-19, 2001.

[24]Rovey, J. L., Gallimore, A. D., "Design and Operation of a Multiple-Cathode, High-Power, Rectangular Discharge Chamber," AIAA-2005-4407, *41st Joint Propulsion Conference*, Tucson, AZ, July 10-13, 2005.

[25]Rovey, J. L., Gallimore, A. D., "Dormant Cathode Plasma Properties and Erosion Analysis in a Multiple-Cathode, High-Power, Rectangular Discharge Chamber," AIAA-2005-4241, *41st Joint Propulsion Conference*, Tucson, AZ, July 10-13, 2005.

[26]Kameyama, I., Wilbur, P. J., "Effects of External Flow near High-Current Hollow Cathodes on Ion-Energy Distributions," IEPC-97-173, *25th International Electric Propulsion Conference*, Cleveland, OH, Aug. 24-28, 1997.

[27]Sovey, J. S., Patterson, M. J., "Ion Beam Sputtering in Electric Propulsion Facilities," AIAA-91-2117, *27th Joint Propulsion Conference*, Sacramento, CA, June 24-27, 1991.

[28]Domonkos, M. T., "Evaluation of Low-Current Orificed Hollow Cathodes," Doctoral Thesis, Dept. of Aerospace Engineering, University of Michigan, Ann Arbor, MI, 1999.

[29]Boyd, I. D., Dressler, R. A., "Far field modeling of the plasma plume of a Hall thruster," *Journal of Applied Physics*, Vol. 92, No. 4, pp. 1764-1774, Aug. 2002.

Appendix

Configuration	DCA	I_d (A)	V_d (V)	Mass Flow, DCA (sccm)	Mass Flow, Anode (sccm)	I_{emag} (A)	DC Electrical Connectivity	DC Flow Rate
0LI	Left	30	24.5	6.12	30.9	0	Isolated	No Flow
0MI	Center	30	24.4	5.73	30.9	0	Isolated	No Flow
5LI	Left	30	25.8	6.12	30.9	5	Isolated	No Flow
5MI	Center	30	25.5	5.73	30.9	5	Isolated	No Flow
10LI	Left	30	28.2	6.12	30.9	10	Isolated	No Flow
10MI	Center	30	27.3	5.73	30.9	10	Isolated	No Flow
0LIH	Left	30	24.5	6.12	30.9	0	Isolated	Half DCA
0MIH	Center	30	24.4	5.73	30.9	0	Isolated	Half DCA
5LIH	Left	30	25.8	6.12	30.9	5	Isolated	Half DCA
5MIH	Center	30	25.5	5.73	30.9	5	Isolated	Half DCA
10LIH	Left	30	28.2	6.12	30.9	10	Isolated	Half DCA
10MIH	Center	30	27.3	5.73	30.9	10	Isolated	Half DCA
0LIF	Left	30	24.5	6.12	30.9	0	Isolated	Full DCA
0MIF	Center	30	24.4	5.73	30.9	0	Isolated	Full DCA
5LIF	Left	30	25.8	6.12	30.9	5	Isolated	Full DCA
5MIF	Center	30	25.5	5.73	30.9	5	Isolated	Full DCA
10LIF	Left	30	28.2	6.12	30.9	10	Isolated	Full DCA
10MIF	Center	30	27.3	5.73	30.9	10	Isolated	Full DCA

Table 4: MCDC TA operational configurations.